Fe and Zn co-substituted beta-tricalcium phosphate (TCP): Synthesis, structural, magnetic, mechanical and biological properties

Lauryna Sinusaite[1], Anton Popov[1,2], Andris Antuzevics[3], Kestutis Mazeika[4], Dalis Baltrunas[4], Jen-Chang Yang[5], Shengfang Shi[6], Tohru Sekino[6], Aivaras Kareiva[1], Aleksej Zarkov[1,*]

[1]*Institute of Chemistry, Vilnius University, Naugarduko 24, LT-03225 Vilnius, Lithuania*

[2]*Department of Immunology, State Research Institute Centre for Innovative Medicine, Santariskiu 5, LT-08406 Vilnius, Lithuania*

[3]*Institute of Solid State Physics, University of Latvia, Kengaraga 8, LV-1063 Riga, Latvia*

[4]*State Research Institute Center for Physical Sciences and Technology, Vilnius LT-02300, Lithuania*

[5]*Graduate Institute of Nanomedicine and Medical Engineering, College of Biomedical Engineering, Taipei Medical University, 250 Wu-Hsing St, Taipei 11052, Taiwan*

[6]*The Institute of Scientific and Industrial Research, Osaka University, 8–1 Mihogaoka, Ibaraki, Osaka 567–0047, Japan*

**Corresponding author: E-mail: aleksej.zarkov@chf.vu.lt; +37062190153*

Abstract

In the present work, Fe^{3+} and Zn^{2+} co-substituted β-tricalcium phosphate (β-TCP) has been synthesized by wet co-precipitation method. Co-substitution level in the range from 1 to 5 mol% has been studied. Thermal decomposition of as-prepared precipitates was shown to be affected by introducing of foreign ions, which decreases precursor decomposition temperature. It was determined that partial substitution of Ca by Fe^{3+} and Zn^{2+} ions leads to the change in lattice parameters, which gradually decrease as doping level increases. Lattice distortion was also confirmed by means of Raman spectroscopy, which showed gradual change of the shape of the spectra. Rietveld refinement and electron paramagnetic resonance study confirmed that Fe^{3+} ions occupies only one Ca crystallographic site until Fe^{3+} and Zn^{2+} substitution level reaches 5 mol%. All co-substituted samples revealed paramagnetic behavior, magnetization of powders was determined to be linearly dependent on concentration of Fe^{3+} ions. Cytotoxicity of the synthesized species was estimated by *in vivo* assay using zebrafish (*Danio rerio*) and revealed non-toxic nature of the samples. Preparation of ceramic bodies from the powders was performed, however the results obtained on Vickers hardness of the ceramics did not show improvement in mechanical properties induced by co-substitution.

Keywords: beta-tricalcium phosphate, TCP, Fe^{3+} and Zn^{2+} co-substitution, structural analysis, cytotoxicity.

1. Introduction

Calcium phosphates (CPs) are the main inorganic part of biological hard tissues such as bones and teeth. This reason makes synthetic CPs widely used in medicine for repair and reconstruction of diseased or damaged parts of bone. For these purposes CPs can be used in different forms varying from thin coatings on metallic implants, used to aid implant fixation into bone, to sintered bioceramics, to be used as synthetic bone graft substitutes [1-3]. Despite the fact that inorganic part of bones mainly consists of calcium hydroxyapatite (HAp, $Ca_{10}(PO_4)_6(OH)_2$), other CPs are also widely used for biomedical purposes. One of the most frequently used CP used for the fabrication of bioceramics is tricalcium phosphate (TCP, $Ca_3(PO_4)_2$), which attracts practical interest due to several reasons such as excellent biocompatibility, osteoconductivity and chemical composition similar to natural bone [4]. Low-temperature β-TCP polymorph crystallizes in the rhomgohedral crystal sistem with the space group R3c. For the fabriication of bioceramics it is usually used in its pure form or as a mixture with HAp, resulting in biphasic bioceramics [5].

Partial substitution of Ca by other biologically active ions has been proposed as a promising tool to the superior biological performance of CP-based materials [6]. Moreover, it can drastically affect physiochemical, mechanical, and anti-bacterial properties. Importance of this approach has been underlined in a number of recent reviews [7-9]. Substitution-induced extra properties allow to combine biocompatibility of CPs with other properties resulting in specific application such as bioimaging, drug delivery...

in recent years, CPs have been strategically integrated with imaging contrast agents and therapeutic agents for various molecular imaging

modalities including fluorescence imaging, magnetic resonance imaging, ultrasound imaging or multimodal imaging, as well as for varioustherapeutic approaches including chemotherapy, gene therapy, hyperthermia therapy, photodynamictherapy, radiation therapy, or combination therapy, even imaging-guided therapy [10].

This approach goes hand in hand with morphological and compositional modification of CPs by partial substitution of Ca with other functional ions.

When multiple ions are doped into hydroxyapatite they alter the atomic structure synergistically. Dopants cause changes in morphology, density, strength, solubility and ion release kinetics of hydroxyapatite.[11]

In the present work, Fe^{3+} and Zn^{2+} were chosen due to the significant performance enhancement that these elements can deliver. Fe is an essential element. It can be found in the structure of many enzymes, which are involved in oxygen trasport, electron trasport, oxidation-reduction and other biological processes in human body [12]. Moreover, as a trace element Fe is also present in natural bones and teeth [13]. Additional interest Fe causes because of its magnetic properties. Previous studies demonstrated that partial substitution of Ca by Fe ions in synthetic CPs can result in materials with multifunctional properties. Superparamagnetic Fe-doped CPs were successfully utilized *in vivo* as imaging agents for magnetic resonance and nuclear imaging [14]. Moreover, feasibility of applilication of Fe^{3+}-doped HAp and iron oxide nanoparticles coated whith amorphous CP for the intracellular hyperthermia of cancers of bone and brain was shown [15]. Another work demonstrated that Fe-doped HAp could be used as functional nano-carriers for the magnetically assisted delivery of bioactive molecules [16].

Zinc is the second most abundant trace element in the human body, which is required for the functioning of many enzymes [17]. Zn-containing CPs have shown enhanced bioactivity and promotion of growth of adipose-derived mesenchymal stem cells [18]. Moreover, antibacterial properties of Zn-substituted CPs were reported in a number of previous works showing inhibitory effect towards pathogenic microorganisms [19].

Despite the fact that different CPs were doped with a huge variety of ions, co-doping of CPs still remains relatively new approach, which aims to use the synergistic effect of multi-element dopants.

Since single doping brings so many opportunities for applications of CPs, it makes sense to combine different dopants for multifunctioning of CP-based materials [11].

The main goal of the present work was to synthesize and characterize β-TCP bioceramics with magnetic and antibacterial properties. Due to this reason β-TCP partially substituted with Fe^{3+} and Zn^{2+} was chosen and series of products with different substitution level was investigated in details.

Co-doped Hap, antibacterial properties [20]

Calcium-based biomaterials for diagnosis, treatment, and theranostics [10]

Cationic Substitutions in Hydroxyapatite: Current Status of the Derived Biofunctional Effects and Their In Vitro Interrogation Methods [8]

Fabrication, Properties and Applications of Dense Hydroxyapatite: A Review [21]

Apie metalus pacituoti, Zn ir Fe [22]

Sintering, hardness [23]

2. Materials and methods

2.1. Synthesis

β-TCP powders substituted with equal amounts of Fe^{3+} and Zn^{2+} ions were synthesized by simple co-precipitation method. Series of compounds containing Fe^{3+} and Zn^{2+} ions in the range from 0 to 5 mol% with a step of 1 mol% were studied in the present work. For the synthesis calcium nitrate tetrahydrate ($Ca(NO_3)_2 \cdot 4H_2O$, ≥99%, Roth), iron(III) nitrate nonahydrate ($Fe(NO_3)_3 \cdot 4H_2O$, ≥98%, Alfa Aesar), zinc(II) nitrate hexahydrate ($Zn(NO_3)_2 \cdot 4H_2O$, ≥98%, Chempur) and diammonium hydrogen phosphate ($(NH_4)_2HPO_4$, ≥98%, Roth) were used as starting materials. Firstly, an appropriate amount of $(NH_4)_2HPO_4$ was dissolved in deionized water to obtain a 0.5 M solution, to which concentrated ammonia solution (NH_4OH, 25%, Roth) was added under constant stirring, pH of the obtained solution was adjusted to 9. Next, an aqueous solution containing appropriate amounts of Ca, Fe and Zn nitrates (total metal ions concentration was 0.75 M) was rapidly added to the above mixture resulting in the instantaneous formation of precipitates. The obtained precipitates were stirred in the reaction mixture for 10 minutes, afterwards filtered, washed with deionized water and dried at 50 °C overnight in the oven. Finally, dry powders were ground in agate mortar and annealed in a furnace at 800 °C temperature for 5 h in air atmosphere with a heating rate of 5 °C/min. For the preparation of β-TCP ceramics polyvinyl alcohol was used as a binder. Powders were uniaxially pressed in 15 mm die and sintered at 1100 °C for 5 h in air atmosphere.

2.2. Characterization

Thermal decomposition of the as-prepared precipitates was analyzed through thermogravimetric (TG) analysis using Perkin Elmer STA 6000 Simultaneous Thermal Analyzer. Dried samples of about 10 mg were heated from 25 to 900 °C with a heating rate of 10 °C/min in a dry flowing air (20 mL/min). Powder X-ray diffraction analysis was performed using Ni-filtered Cu Kα radiation on Rigaku MiniFlex II diffractometer working in Bragg-Brentano (θ/2θ) geometry. The data were collected within 2θ range from 10 to 110° at a step width of 0.01° and speed of 1°/min. Lattice parameters were refined by the Rietveld method using the FullProf suite in the profile matching mode.

Fourier transform infrared spectra (FTIR) were taken in the range of 3000-400 cm^{-1} with Perkin Elmer Frontier ATR-FTIR spectrometer equipped with a liquid nitrogen cooled MCT detector. Raman spectra were recorded at room temperature using combined Raman and scanning near field optical microscope (SNOM) WiTec Alpha 300 R equipped with 532 nm excitation laser source. Morphological features of the synthesized products were analyzed with a Hitachi SU-70 field-emission scanning electron microscope (FE-SEM). Quantitative elemental analysis of the samples was carried out using Perkin Elmer Optima 7000DV inductively coupled plasma optical emission spectrometer (ICP-OES). The analyzed powders were dissolved in nitric acid (HNO_3, Rotipuran® Supra 69%, Carl Roth) and diluted with deionized water. Room temperature electron paramagnetic resonance (EPR) spectra were measured with Bruker ELEXSYS-II E500 CW-EPR spectrometer. Power of 9.46 GHz microwaves was set at 0.6325 mW. The magnetic field was modulated at 100 kHz with 0.4 mT modulation amplitude. EPR signal intensities have been normalized to the sample mass. Dependence of magnetization of samples on the strength of magnetic field were recorded using magnetometer consisting of the lock-in amplifier SR510 (Stanford Research Systems), the gauss/teslameter FH-54 (Magnet Physics) and the laboratory magnet supplied by the power source SM 330-AR-22 (Delta Elektronika). Mössbauer spectra were measured in transmission geometry using ^{57}Co(Rh) source and Mössbauer spectrometer (Wissenschaftliche Elektronik GmbH) at room temperature and low temperature (>10 K) applying closed cycle He cryostat (Advanced Research Systems). Density of the sintered pellets was measured by Archimedes' method in water. Vickers hardness of the prepared β-TCP ceramics was measured using Future-Tech Vickers hardness tester FV-310e. Ten indentations of a single load of 1 N were used for the pellets of each composition.

Cytotoxicity

3. Results and discussion

Thermogravimetric analysis of pristine and Fe/Zn co-substituted as-prepared precipitates was performed in order to investigate thermal behavior of precursor powders and estimate minimal required annealing temperature. TG/DTG curves corresponding to non-substituted sample and sample co-substituted with the highest content of Fe and Zn ions are shown in Fig. 1 as representative.

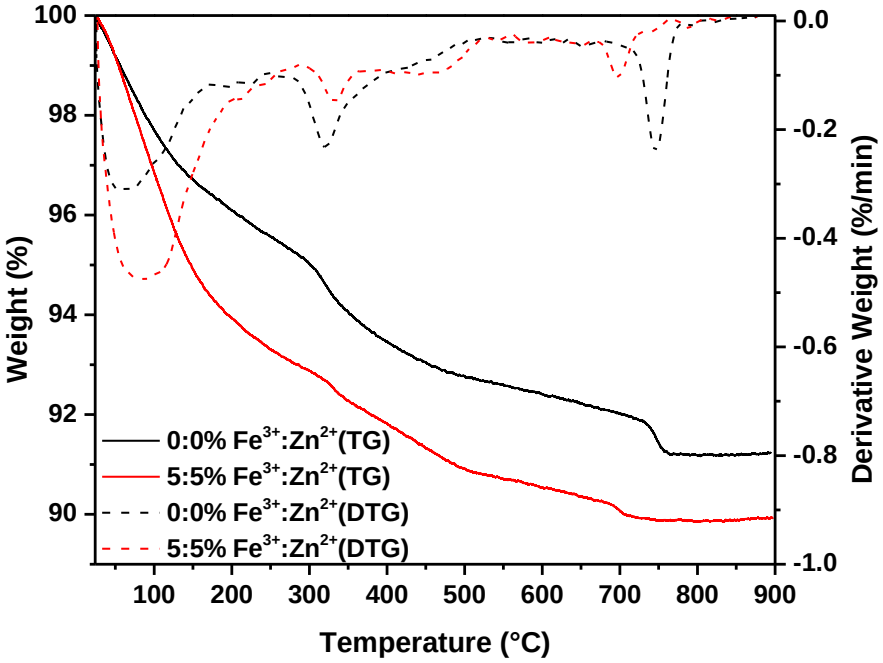

Fig. 1. TG/DTG curves of dried as-prepared precipitates with 0 and 5:5 mol% of Fe and Zn.

It is seen that for both samples thermal decomposition occurs in a very similar way, however it is obvious that presence of foreign ions reduces final decomposition temperature of precursors. For pristine precipitates residual mass is constant at above 775 °C, whereas for substituted sample this temperature is lowered by approximately 50 °C, which is clearly seen from DTG curves. Total weight loss, attributed to the removal of adsorbed and crystalline water and possible residuals of ammonium nitrate, was determined to be 8.8 and 10% for pure and substituted precipitates, respectively. Based on the results of thermal analysis an identical annealing temperature of 800 °C was chosen for all samples.

The phase crystallinity and purity of annealed powders were characterized by XRD analysis. The XRD patterns of the powders containing different amounts of substituent ions and annealed at 800 °C are given in Fig. 2.

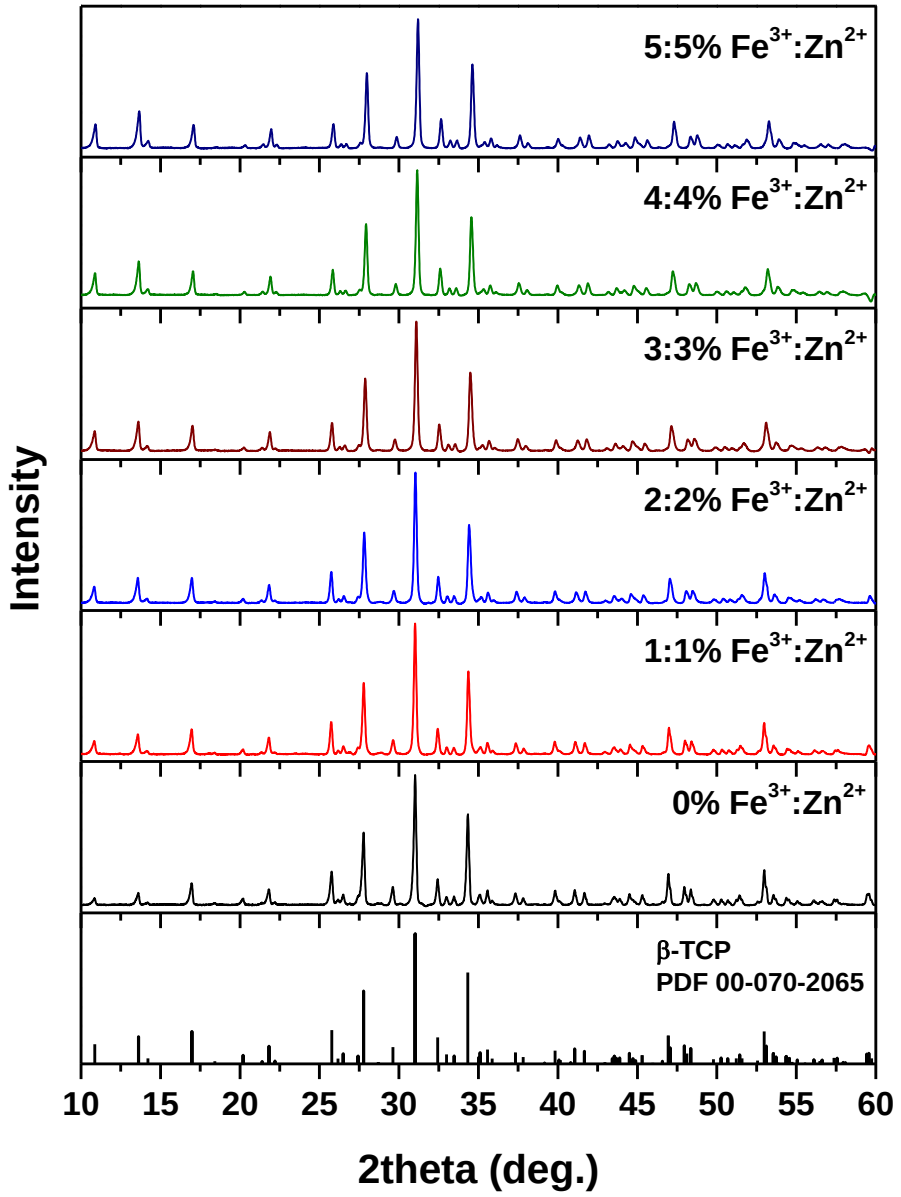

Fig. 2. XRD patterns of β-TCP powders with different amounts of Fe and Zn.

Regardless of chemical composition all synthesized products crystallized to β-TCP phase. All diffraction peaks match very well standard XRD data of rhombohedral $Ca_3(PO_4)_2$ (ICDD 00-070-

2065) and no reflections assigned to potential secondary crystal phases such as Fe or Zn phosphates were detected. Closer look at the diffraction patterns reveals gradual shift of diffraction peaks towards higher 2θ values. Displacement of the particular peak is illustrated in Fig. S1 as representative. Such changes in the XRD patterns are explained by the mismatch in size between Ca and foreign ions and can be considered as an evidence of successful incorporation of substituent ions into β-TCP crystal lattice. Ionic radius of Ca^{2+} in six-fold coordination is 0.1 nm, and ionic radii of both Fe^{3+} and Zn^{2+} ions are significantly smaller – 0.65 and 0.74 nm, respectively [24]. Dependence of calculated lattice parameters on substitution level in β-TCP powders is depicted in Fig. 3.

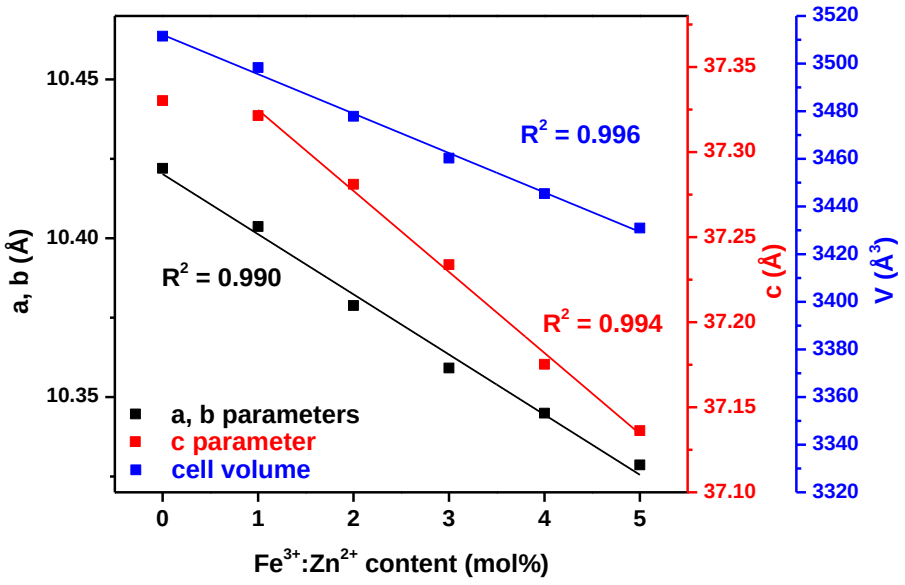

Fig. 3. Lattice parameters of TCP powders with different amounts of Fe and Zn.

It is evident that lattice parameters a and b gradually decrease as substitution level increases. The decrease is linear, what is in line with R^2 values of linear fit of experimental data being close to unity. Slightly different behavior was observed for parameter c, which shows linear decrease only for samples with Fe and Zn content level ranged from 1 to 5 mol%, while parameter c of pristine β-TCP is out of this trend. This suggests that initially cell volume reduces mostly due to the changes of crystal lattice in a and b directions. Similar change in lattice parameter c was previously reported by Mellier *et al.* for Ga-substituted β-TCP [25]. Rietveld refinement showed that foreign ions preferably occupy Ca(5) site in crystal lattice up to 4 mol% co-substitution level. Occupation of this site is in

good agreement with previously reported theoretical and experimental studies on substituted β-TCP, which is characterized by low defect formation energies for small guest cations on octahedral Ca(5) site [26-28]. With the highest substitution level part of foreign ions also occupy Ca(4) site, which is also in good agreement with previously reported data for highly doped β-TCP [29, 30].

Vibrational spectroscopy was also employed to investigate the effect of substitution and check the presence of neighboring amorphous or crystalline materials, which are hardly detectable by XRD analysis in the presence of major β-TCP phase. Raman spectra of the synthesized β-TCP powders are depicted in Fig. 4.

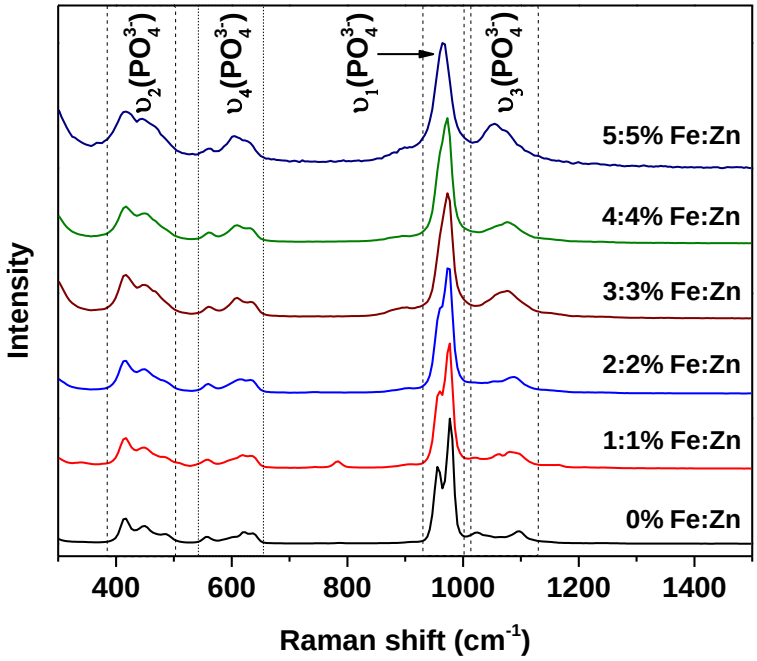

Fig. 4. Raman spectra of TCP powders with different amounts of Fe and Zn.

Four main groups of signals are clearly seen for all analyzed compounds. All obtained spectra are dominated by ν1 vibration mode located in the range of 930-1000 cm^{-1}. Other groups are seen in the range of approximately 385-500, 540-655 and 1015-1130 cm^{-1} and attributed to ν2, ν4, and ν3 modes, respectively [31, 32]. It is obvious that shape of Raman spectra is gradually changes as content of Fe and Zn ions increases. The splitted peak assigned to ν1 vibration mode for highly substituted samples is broadened and transformed into the single peak indicating lattice distortion induced by incorporation of foreign ions. Other signals with increase of substitution level also lose their well-

defined shape and broadened. Week signal at around 785 cm^{-1} is assigned to calcium pyrophosphate secondary phase, which is frequently found as an impurity in β-TCP powders prepared by precipitation method [33, 34].

Fig. 5 shows FTIR spectra of the synthesized powders. The wavenumber range of 1500-400 cm^{-1} was selected to demonstrate the absorption bands of representative functional groups.

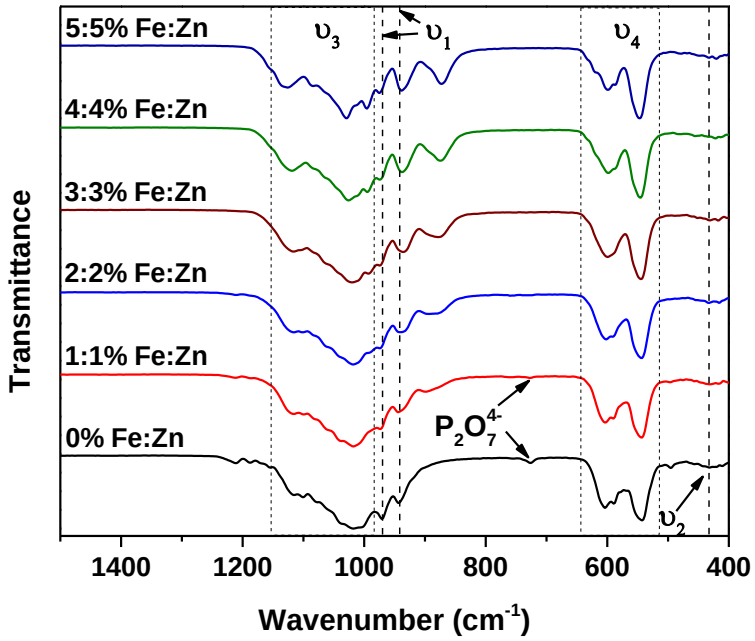

Fig. 5. FTIR spectra of TCP powders with different amounts of Fe and Zn.

All FTIR spectra show vibrational modes characteristic to phosphate groups in β-TCP crystal structure. Four groups of absorption bands are clearly visible and distinguishable. Broad bands located at 1150-990 and 645-515 cm^{-1} are assigned to phosphate ν3 stretching mode and ν4 bending mode, respectively. Two absorption bands located at 970 and 940 cm^{-1} are ascribed to ν1 mode and weak absorption band centered at around 432 cm^{-1} corresponds to ν1 mode [31]. Additional weak absorption band located at 729 cm^{-1} was observed in FTIR spectra of pristine β-TCP and β-TCP substituted with 1 mol% of foreign ions, however it is not seen in FTIR spectra of the samples with higher substitution level. This band corresponds to $P_2O_7^{4-}$ group and confirms the presence of negligible amount of calcium pyrophosphate [35]. Another clearly visible band can be seen at 873 cm^{-1}. Appearance of this signal is obviously caused by substitution of Ca by foreign ions, since

intensity of this band monotonically increases as substitution level increases. Similar appearance of absorption band was observed in FTIR spectra of other substituted β-TCP powders [28, 36] and potentially could be attributed to HPO_4^{2-} group [37].

Deviation of the actual chemical composition of final products from the target stoichiometry is a well-known issue for the synthesis of multicomponent compounds by co-precipitation method. In order to confirm chemical composition of the synthesized powders, elemental analysis by means of ICP-OES was performed. The results of the analysis are summarized in Table 1.

Table 1. Results of the elemental analysis of the samples performed by ICP-OES.

Sample	$\frac{\mathbf{n(Zn)\cdot 100\%}}{\mathbf{n(Ca+Zn+Fe)}}$	$\frac{\mathbf{n(Fe)\cdot 100\%}}{\mathbf{n(Ca+Zn+Fe)}}$
1:1% Fe:Zn	1.03	0.966
2:2% Fe:Zn	1.93	1.81
3:3% Fe:Zn	3.27	2.86
4:4% Fe:Zn	4.01	3.71
5:5% Fe:Zn	5.26	4.68

Determined molar percentage of the substituents is in good agreement with nominal values and monotonically increases as theoretical substitution level increases. On the other hand, there is a notable trend, that for all samples amount Fe is regularly lower than theoretical, however, this mismatch is not significant and does not exceed 10%. In combination with XRD, Raman and FTIR data, elemental analysis indicates that suggested synthetic approach is suitable for the preparation of Fe and Zn co-substituted β-TCP powders with good phase purity and controllable composition.

Room temperature EPR spectra of the investigated samples are depicted in Fig. 6.

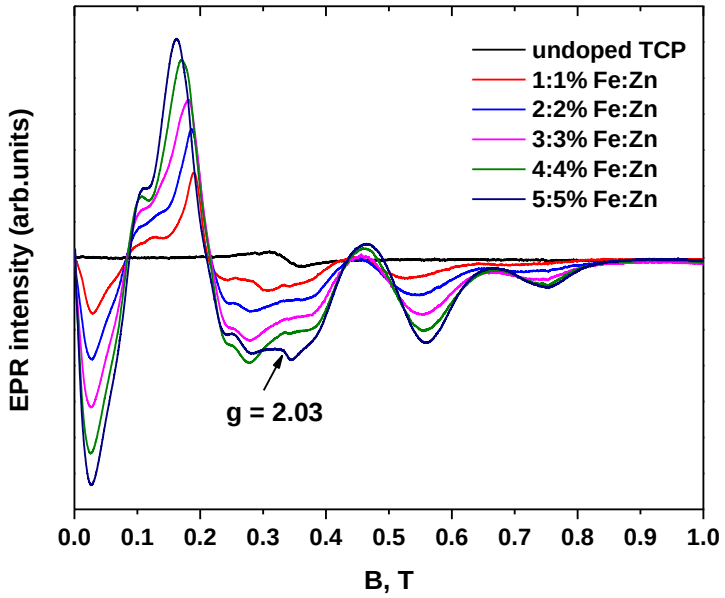

Fig. 6. EPR spectra of TCP powders with different amounts of Fe and Zn.

A relatively low intensity Lorentzian-shape signal with peak-to-peak linewidth of around 50 mT centered at $g \approx 2.00$ is present in the spectrum of non-substituted sample. It indicates the presence of a small ammount of paramagnetic centers, which are not related to Fe^{3+} impurities. Moreover, Zn only containing β-TCP powders did not reveal any EPR signals different from that arised from pristine β-TCP. The Fe-containing samples expectedly exhibited EPR spectra characteristic to the Fe^{3+} valence state. The electron spin of Fe^{3+} is $S = 5/2$, thus, in addition to the Zeeman effect, zero field splitting (ZFS) of the ground state is also expected. If the magnitude of ZFS is large, it is reflected in an EPR signal, which spans a wide magnetic field range [38]. EPR signal intensities scale with Fe content in the samples, which suggests that regardless of the substitution level Fe^{3+} is the preferrable charge state in this matrix. The shape of the signal becomes broader and there is a systematic shift in the major peak position as the Fe content increases. The additional broadening is most likely a consequnce of increased dipole-dipole interactions of nearby paramagnetic centers [39]. The EPR resonance positions of high S systems are determined by the values of ZFS parameters, therefore a shift in peaks of powder spectra indicates variations in the parameter values and their distributions [40]. This, in turn, implies concentration-dependent distortions in the Fe^{3+} local structure from site to site, which could be associated with slight changes in Fe-O distances and bond angles as well as

increased long-range disorder in the β-TCP crystal structure. No significant changes are observed in the relative intensities of the spectral features up to 5 mol% co-substitution. It indicates that Fe^{3+} ions either occupy one unique position in the crystal structure or are distributed across several site positions in similar proportions regardless of Fe^{3+} content. Taking into account previous investigations, which suggested that incorporation of Fe^{3+} ions in β-TCP occurs via substitution in Ca(5) and Ca(4) sites of the crystal lattice [41, 42] and results of XRD analysis, the most plausible explanation is that the observed EPR signals originate from Fe^{3+} ions in the Ca(5) position. An additional weaker signal at $g \approx 2.03$ can be observed in the sample with 5 mol% substitution level and could be related to Fe^{3+} ions substituting Ca^{2+} ions in Ca(4) position, however at high doping levels formation of more complicated paramagnetic structures cannot be ruled out. Recent studies of Fe-doped β-TCP system [28, 30] have presented EPR spectra, which consisted of two major features located at $g = 4.27$ and 2.08. The reported spectra bear resemblance to Fe^{3+} EPR spectra in glasses [43-45] and are quite different from our obtained results. While it is difficult to comment on the specifics of the spectra, it clearly demonstrates that incorporation of Fe^{3+} ions in the β-TCP structure is sensitive to the substitution level as well as synthesis conditions.

Room temperature dependence of magnetization of β-TCP powders of all compositions on applied magnetic field strength is illustrated in Fig. 7.

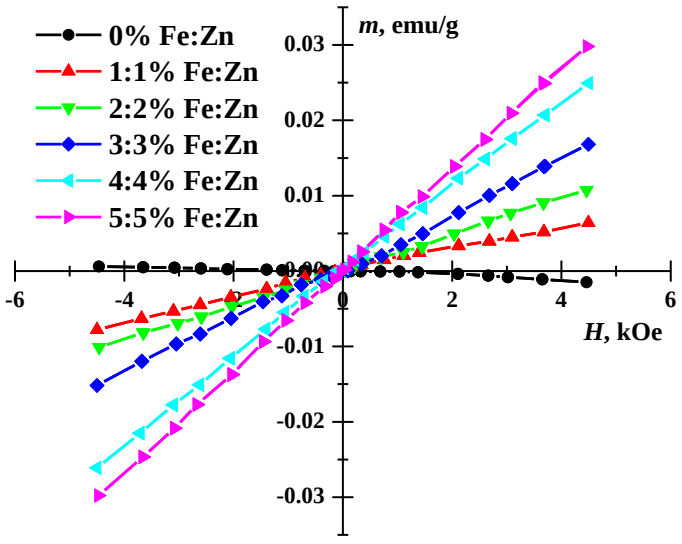

Fig. 7. Magnetization dependence on magnetic field strength for TCP powders with different amounts of Fe and Zn.

Different magnetic behavior of β-TCP samples depending on the presence of foreign ions is evident. Pristine sample shows weak diamagnetic properties, wich is in agreement with previously reported data on magnetic properties of undoped HAp and β-TCP [46-48]. Different behavior is observed for Fe and Zn-containing powders, which clearly exhibit paramagnetic behavior. Magnetization values are linearly proportional to applied magnetic field strength, moreover magnetization obviously increases as Fe content in the samples increases. No saturation of magnetization was observed regardless of chemical composition of the samples in studied magnetic field range.

Mössbauer spectra of selected Fe-containing β-TCP samples measured at different temperatures and magnetic fields are presented in Fig. 8.

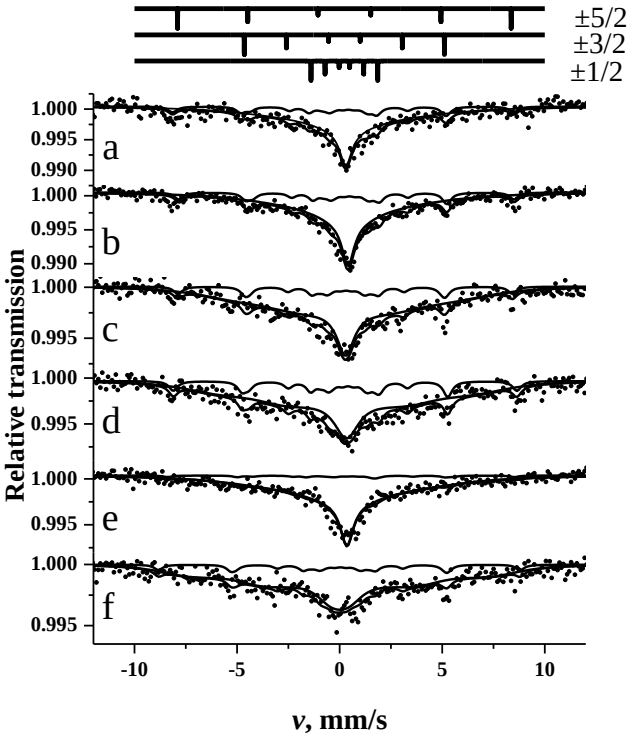

Fig. 8. Mössbauer spectra of 5:5% Fe:Zn-TCP (a,b,c), 4:4% Fe:Zn-TCP (d), 3:3% Fe:Zn-TCP (e), 5:5% Fe:Zn-TCP measured at 11 K (a) and room temperature (b-f) at applied magnetic field B=0 T (a,b,e) and B=0.42 T (c,d,f).

Broadened magnetic structure of Mössbauer spectra shows that Fe^{3+} spins experience dynamics, which characteristic time is within 10^{-7}-10^{-9} s time range, where Mössbauer spectroscopy is sensitive

to hyperfine interactions changes. Hyperfine magnetic structure of Mössbauer spectra of paramagnetic Fe^{3+} is observed when paramagnetic ions are diluted [49]. It was observed that Mössbauer spectra of β-TCP samples at low temperature and room temperature are quite similar. The shape of Mössbauer spectra can be explained by the influence of spin-spin relaxation which has weak dependence on temperature whereas the spin-lattice relaxation is obviously temperature-dependent.

Fe^{3+} spin Hamiltonian is a sum of contributions of interactions with crystal field, Zeeman interaction with magnetic field, and magnetic dipole interactions [49]. Exchange interactions between spins which could result in the magnetic ordering are not present when Fe ions are diluted in a non-magnetic matrix. The application of magnetic field may have considerable influence on spectra and can help to simplify the analysis of Mössbauer spectra if the interaction with magnetic field would become stronger than with existing crystal field. However, the applied magnetic field of 0.42 T (perpendicularly the gamma rays) was not sufficient to fully distinguish the magnetic structure of Mössbauer spectra.

Influence of relaxation on Mössbauer spectra was expressed in simplified form using multistate relaxation model [50, 51] when nuclear Hamiltonian is diagonal for all stochastic spin states considering that magnetic hyperfine interaction is much stronger than quadrupole one. The line shape was separately expressed for each nuclear transition defining the static line positions of spectrum v_i:

$$I(\omega) = 2\,\mathrm{Re}\left(\mathbf{P}\cdot\left(\left(i\left(v - v_i\right) - \Gamma/2\right)\cdot\mathbf{I} - \mathbf{W}\right)^{-1}\cdot\mathbf{1}\right) \quad (1)$$

Probabilities of stochastic spin states which were defined by vector **P** components were taken to be equal. **I** was diagonal unit matrix and **1** is column vector with all components equal to unity. Tridiagonal matrix **W** defined transition probabilities between stochastic states. The transition probability from i to j state was given by matrix element W_{ij} and the diagonal element $W_{ii} = -\sum_{j\neq i} W_{ij}$ [50].

The spin relaxation can be sufficiently well characterized by Fe^{3+} spin states $S_z = \pm\frac{5}{2};\pm\frac{3}{2};\pm\frac{1}{2}$ when sextets have splitting ratios of approximately 5:3:1 [49]. Positions of the lines of sextets

corresponding to the hyperfine field of 50.5 T and S_z values are shown in Fig. 8. The probability corresponding to $S_z - S_z \pm 1$ transition is $W_{S_z S_z \pm 1} = \left(S(S+1) - S_z(S_z \pm 1)\right) \cdot R$ where R is relaxation rate. With increase in relaxation rate in the range of 10^7-10^{10} s^{-1} the shape of Mössbauer spectrum lines changes causing rise of intensity at the center of spectrum.

As observed, smaller part of Mössbauer spectra, up to 19% of all area (see Table 2), can be attributed to Fe spins, which relax with slower rates in comparison to Mössbauer spectroscopy sensitivity limit (R<10^7 s^{-1}) and gives expressed hyperfine magnetic structure of spectra attributable to S_z states. The clearly observed sextet with hyperfine field B_h≈50 T is attributed to $S_z = \pm\frac{5}{2}$. The isomer shift δ≈0.4 mm/s relatively to α-Fe is characteristic of Fe^{3+}. Spin-spin relaxation is explained by cross relaxation processes [49] when the increase in Zeeman and crystal field energies of one spin is accompanied by almost equal decrease in energy of another spin. The results obtained by fitting Mössbauer spectra (see Table 2) indicate that the application of magnetic field of 0.42 T causes considerable decrease in relaxation rate R. It can be noted that applied magnetic field determines changes in energy related to spin states depending on the magnetic field direction relatively to the main axis of crystal field.

Table 2. Parameters of fitting of Mössbauer spectra measured at temperature T and applied magnetic field B_{appl}. R is relaxation rate, S is relative area of spectrum attributed to slow relaxation (R=0). δ is isomer shift relatively to α-Fe, 2ε is quadrupole shift and B_h is hyperfine field.

Sample	***T*, K**	B_{appl}**, T**	***R*, 10^8 s^{-1}**	***S*,% ±1**	δ**, mm/s**	B_h**, T**	2ε**, mm/s**
5:5% Fe:Zn	11	0	2.7±0.4	19	0.41±0.03	51.6±0.7	0.13±0.1
5:5% Fe:Zn	296	0	2.9±0.3	19	0.52±0.03	50.8±0.3	0.08±0.06
5:5% Fe:Zn	296	0.42	1.14±0.15	15	0.40±0.04	50.5*	0.0*
4:4% Fe:Zn	296	0.42	0.73±0.15	19	0.44±0.03	52.0±0.03	0.07±0.04
3:3% Fe:Zn	296	0	2.3±0.3	4	0.45±0.05	50.5*	0.0*
3:3% Fe:Zn	296	0.42	0.46±0.09	13	0.49±0.1	48.6±1.6	-0.08±0.08
2:2% Fe:Zn	296	0.42	0.33±0.06	11	0.38±0.05	50.5*	0.0*
1:1% Fe:Zn	296	0.42	0.51	16	0.38*	50.5*	0.0*

* fixed value

In β-TCP crystal structure Fe^{3+} ions substitute Ca ones [42] while in Fe-doped hydroxyapatite the differently coordinated Fe^{3+} interstitial sites can be found to be located in the hexagonal channel [41]. Mössbauer spectra of hydroxyapatite consist of doublets and hyperfine magnetic structure is not observed at Fe content as low as in $Ca_{10}Fe_{0.15}(PO_4)_6(OH)_{1.55}O_{0.45}$. However, relaxation rate should depend on local Fe concentrations. Properties of Fe sites are also possibly important determining rates of spin-spin and spin-lattice relaxations.

SEM was employed in order to investigate influence of foreign ions and their concentration on morphological features of β-TCP samples. SEM micrographs of pristine β-TCP powders and powders substituted with the highest amount of Fe and Zn are shown in Fig. 9 as representative.

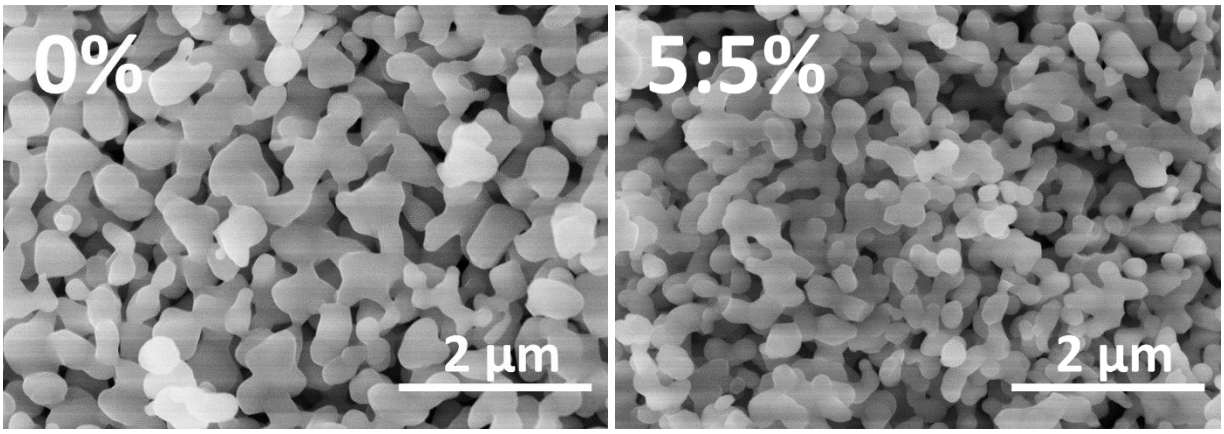

Fig. 9. SEM images of pristine TCP and TCP powders co-substituted with 5 mol% of Fe and Zn.

It is seen that non-substituted β-TCP powders consist of mostly uniform particles of irregular shape, which are highly connected to each other and form porous aggregates. The grain size varies from approximately 200 to 500 nm. Substitution with Fe and Zn does not change porous nature of the aggregated powders, however it obviously affects the grain size, which was reduced significantly. The observed particles showed prolonged irregular shape with thickness of around 150-200 nm and length up to 1 µm.

In order to determine toxicity of the synthesized products, *in vivo* cytotoxicity assay was performed in solutions containing 1 wt% of β-TCP powders using zebrafish embryos. Digital photographs of zebrafish embryos taken at different time of presence in TCP-containing solutions are demonstrated

in Fig. 10. Evidently, embryos grown in different media visually do not differ from control zebrafish embryos, there are no visible hybridizations or anomalies caused by interaction with pristine or co-substituted β-TCP. Detailed data on hatching rate, survival rate and body length of zebrafish embryos grown in solutions with β-TCP powders for 72 h are summarized in Table 3. It is seen that hatching and survival rate for all samples vary in the range of 80 to 100%, which is very close to the values obtained for control species, which are 90% for both parameters. Moreover, there are no trends which could be associated with amount of Fe and Zn in investigated samples. On the other hand there is a visible trend in the body length of the embryos. With the only exception for β-TCP with 1 mol% of Fe and Zn, mean values of the body length of the embryos monotonically increases as a concentration of foreign ions in β-TCP powders increases and exceeds body length of control embryos. Such behavior of zebrafish embryos in TCP-containing media together with an absence of visible anomalies indicate non-toxic nature of the synthesized powders.

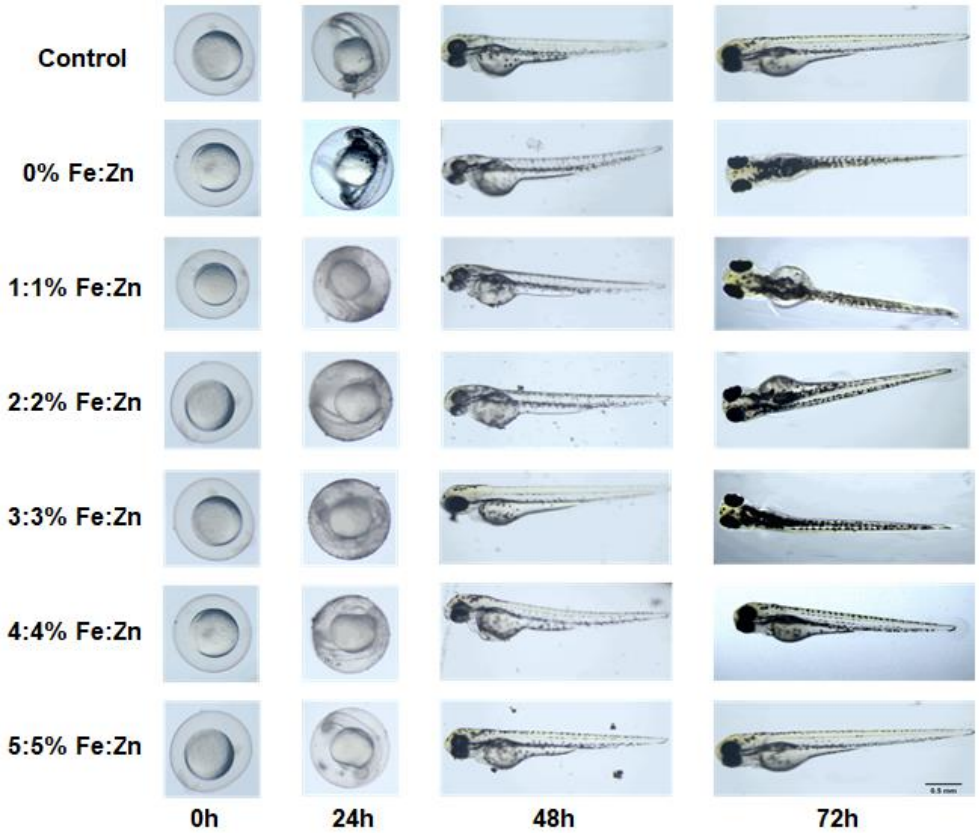

Fig. 10. Digital photographs of zebrafish embryos at different stages of growth in solutions containing TCP powders with different amount of Fe and Zn.

Table 3. Hatching rate, survival rate and body length of zebrafish embryos grown in solutions containing TCP powders for 72 h (N=10).

Sample	Hatching Rate (%)	Survival Rate (%)	Body Length (mm)
E3 Median*	90	90	3.26±0.21
0% Fe:Zn	80	80	3.42±0.24
1:1% Fe:Zn	90	90	3.27±0.42
2:2% Fe: Zn	80	80	3.50±0.27
3:3% Fe: Zn	100	100	3.55±0.24
4:4% Fe: Zn	90	90	3.55±0.13
5:5% Fe:Zn	100	90	3.61±0.17

*E3 medium (5 mM NaCl, 0.17 mM KCl, 0.33 mM $CaCl_2$, 0.33 mM $MgSO_4$, and 0.1% (w/v) methylene blue) for Zebrafish embryos.

All synthesized β-TCP powders were pressed into pellets and sintered in order to prepare ceramic bodies. The XRD patterns of the sintered pellets are shown in Fig. S3. After sintering procedure analyzed samples remained single-phase β-TCP and no additional phases such as high-temperature α-TCP polymorph were observed. Reflection peaks became sharper indicating higher crystallinity and grain growth in ceramic discs in comparison to powders. Fig. 11 represents SEM images of polished and thermally etched surface of pristine β-TCP pellet and β-TCP pellet substituted with 5 mol% of Fe and Zn.

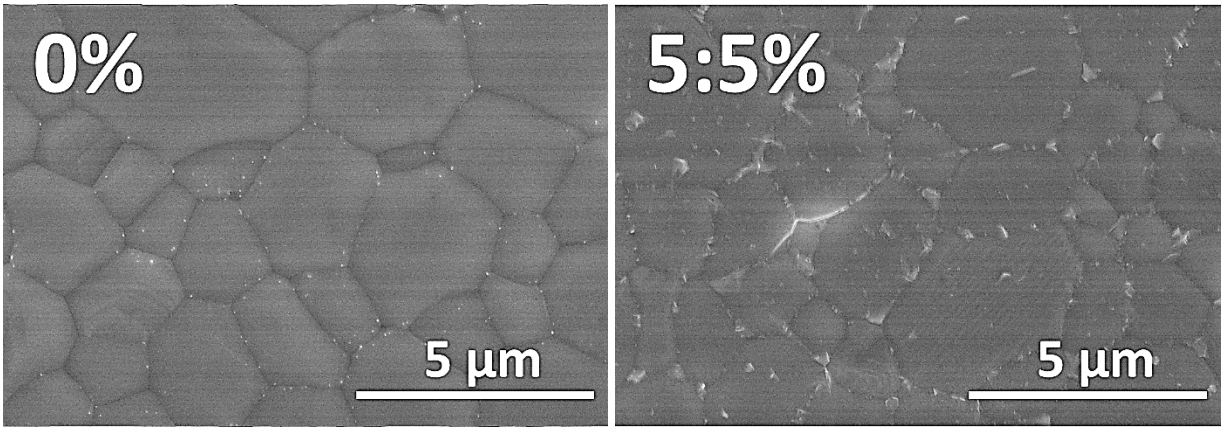

Fig. 11. SEM images of polished and thermally etched surface of pristine TCP pellet and sample co-substituted with 5 mol% of Fe and Zn and sintered at 1100 °C.

Surface of pure β-TCP pellet is composed of the grains varying in size in the range of approximately 1.5 to 7 μm. No cracks, holes or other clearly visible defects were observed. Substitution with foreign ions did not suppress or promote grain growth, which remained nearly the same in terms of size. Unfortunately, the highest substitution level resulted in formation of some visible cracks, moreover some deposits were observed in the grain boundaries. Linear shrinkage, densities and Vickers hardness of sintered β-TCP pellets are given in Table 4.

Table 4. Linear shrinkage, density and Vickers hardness of TCP ceramics.

Sample	Linear shrinkage (%)	Density (%)	Vickers hardness (GPa)
0% Fe:Zn	13	95	4.05±0.27
1:1% Fe:Zn	11	93	3.08±0.18
2:2% Fe: Zn	8	91	1.82±0.05
3:3% Fe: Zn	14	94	2.66±0.06
4:4% Fe: Zn	15	102	2.87±0.11
5:5% Fe:Zn	16	102	2.60±0.06

It was observed, that linear shrinkage of the sintered pellets did not correlate with substitution level. Linear shrinkage was determined to be the highest for powders with 5 mol% of foreign ions and the lowest for powders with 2 mol% of Fe and Zn. Measured densities of the sintered species based on theoretical density of β-TCP (3.07 g/cm^{-3} [4]) also did not reveal any trends and varied in the range from 88 to 102% with the highest value for pellets with the highest substitution level. Vickers hardness measurements did not reveal improvement in mechanical properties of the prepared ceramics induced by substitution of Ca ions. Determined average Vickers hardness ranged from 1.81 to 4.05 GPa, however the highest value was observed for pristine β-TCP ceramics and was in good agreement with previously reported values [23, 52, 53]. The obtained results indicate, that while partial substitution of Ca with Fe and Zn resulted in phase pure, non-toxic and magnetic powders, this approach did not lead to superior mechanical properties.

4. Conclusions

Series of β-TCP powders co-substituted with equal amounts of Fe^{3+} and Zn^{2+} ions in the range of 1-5 mol% have been successfully synthesized by simple and reliable co-precipitation method. Structural analysis revealed gradual decrease in lattice parameters of the synthesized samples with increase of substitution level. XRD and EPR studies showed that both foreign ions preferably occupy octahedral Ca(5) site and Ca(4) at the highest substitution level. Raman spectroscopy confirmed lattice distortion of co-substituted samples by gradual change in shape of the obtained spectra. All substituted samples exhibited paramagnetic behavior, magnetization values were found to be proportional to Fe percentage in the synthesized powders. In vivo cytotoxicity assay did not reveal toxic behavior of the synthesized powders even with the highest content of foreign ions. Mechanical properties of sintered β-TCP pellets were not improved by substitution of Ca by foreign ions. Vickers hardness values were determined to be lower for substituted samples in comparison to those of pristine β-TCP ceramics.

Notes

The authors declare no competing financial interest.

Acknowledgements

This work was supported by the European Social Fund under the No. 09.3.3- LMT-K-712 "Development of Competences of Scientists, other Researchers and Students through Practical Research Activities" measure (grant No. 09.3.3-LMT-K-712-14-0059). AK would like to express sincere gratitude for Fellowship administrated by The Japan Society for the Promotion of Science (JSPS). Fellow's ID No.: L12546. Authors are grateful to R. Vargalis (Vilnius University) for taking SEM images.

References

[1] W. Habraken, P. Habibovic, M. Epple, M. Bohner, Calcium phosphates in biomedical applications: materials for the future?, Mater. Today, 19 (2016) 69-87.
[2] E.A. Chudinova, M.A. Surmeneva, A.S. Timin, T.E. Karpov, A. Wittmar, M. Ulbricht, A. Ivanova, K. Loza, O. Prymak, A. Koptyug, M. Epple, R.A. Surmenev, Adhesion, proliferation, and osteogenic differentiation of human mesenchymal stem cells on additively manufactured Ti6Al4V alloy scaffolds modified with calcium phosphate nanoparticles, Colloids and Surfaces B: Biointerfaces, 176 (2019) 130-139.
[3] S.V. Dorozhkin, Calcium Orthophosphate-Based Bioceramics, Materials, 6 (2013) 3840-3942.
[4] R.G. Carrodeguas, S. De Aza, α-Tricalcium phosphate: Synthesis, properties and biomedical applications, Acta Biomater., 7 (2011) 3536-3546.
[5] M. Ebrahimi, M.G. Botelho, S.V. Dorozhkin, Biphasic calcium phosphates bioceramics (HA/TCP): Concept, physicochemical properties and the impact of standardization of study protocols in biomaterials research, Mater. Sci. Eng. C, 71 (2017) 1293-1312.
[6] E. Boanini, M. Gazzano, A. Bigi, Ionic substitutions in calcium phosphates synthesized at low temperature, Acta Biomater., 6 (2010) 1882-1894.
[7] J.T.B. Ratnayake, M. Mucalo, G.J. Dias, Substituted hydroxyapatites for bone regeneration: A review of current trends, J. Biomed. Mater. Res. B: Appl. Biomater., 105 (2017) 1285-1299.
[8] T. Tite, A.-C. Popa, L.M. Balescu, I.M. Bogdan, I. Pasuk, J.M.F. Ferreira, G.E. Stan, Cationic Substitutions in Hydroxyapatite: Current Status of the Derived Biofunctional Effects and Their In Vitro Interrogation Methods, Materials, 11 (2018) 2081.
[9] M. Šupová, Substituted hydroxyapatites for biomedical applications: A review, Ceram. Int., 41 (2015) 9203-9231.
[10] C. Qi, J. Lin, L.H. Fu, P. Huang, Calcium-based biomaterials for diagnosis, treatment, and theranostics, Chem. Soc. Rev., 47 (2018) 357-403.
[11] B. Yilmaz, A.Z. Alshemary, Z. Evis, Co-doped hydroxyapatites as potential materials for biomedical applications, Microchemical Journal, 144 (2019) 443-453.
[12] N. Abbaspour, R. Hurrell, R. Kelishadi, Review on iron and its importance for human health, J. Res. Med. Sci., 19 (2014) 164-174.
[13] R. Morrissey, L.M. Rodríguez-Lorenzo, K.A. Gross, Influence of ferrous iron incorporation on the structure of hydroxyapatite, J. Mater. Sci. Mater. Med., 16 (2005) 387-392.
[14] A. Adamiano, M. Iafisco, M. Sandri, M. Basini, P. Arosio, T. Canu, G. Sitia, A. Esposito, V. Iannotti, G. Ausanio, E. Fragogeorgi, M. Rouchota, G. Loudos, A. Lascialfari, A. Tampieri, On the use of superparamagnetic hydroxyapatite nanoparticles as an agent for magnetic and nuclear in vivo imaging, Acta Biomater., 73 (2018) 458-469.
[15] A. Adamiano, V.M. Wu, F. Carella, G. Lamura, F. Canepa, A. Tampieri, M. Iafisco, V. Uskokovic, Magnetic calcium phosphates nanocomposites for the intracellular hyperthermia of cancers of bone and brain, Nanomedicine, 14 (2019) 1267-1289.
[16] A. Marrella, M. Iafisco, A. Adamiano, S. Rossi, M. Aiello, M. Barandalla-Sobrados, P. Carullo, M. Miragoli, A. Tampieri, S. Scaglione, D. Catalucci, A combined low-frequency electromagnetic and fluidic stimulation for a controlled drug release from superparamagnetic calcium phosphate nanoparticles: potential application for cardiovascular diseases, J. R. Soc. Interface, 15 (2018) 11.
[17] Y. Cherasse, Y. Urade, Dietary Zinc Acts as a Sleep Modulator, Int J Mol Sci, 18 (2017) 2334.
[18] E.S. Thian, T. Konishi, Y. Kawanobe, P.N. Lim, C. Choong, B. Ho, M. Aizawa, Zinc-substituted hydroxyapatite: a biomaterial with enhanced bioactivity and antibacterial properties, J. Mater. Sci. Mater. Med., 24 (2013) 437-445.
[19] V. Graziani, M. Fosca, A.A. Egorov, Y.V. Zobkov, A.Y. Fedotov, A.E. Baranchikov, M. Ortenzi, R. Caminiti, V.S. Komlev, J.V. Rau, Zinc-releasing calcium phosphate cements for bone substitute materials, Ceram. Int., 42 (2016) 17310-17316.
[20] S. Sprio, L. Preti, M. Montesi, S. Panseri, A. Adamiano, A. Vandini, N.M. Pugno, A. Tampieri, Surface Phenomena Enhancing the Antibacterial and Osteogenic Ability of Nanocrystalline

Hydroxyapatite, Activated by Multiple-Ion Doping, ACS Biomater. Sci. Eng., DOI 10.1021/acsbiomaterials.9b00893(2019).
[21] M. Prakasam, J. Locs, K. Salma-Ancane, D. Loca, A. Largeteau, L. Berzina-Cimdina, Fabrication, Properties and Applications of Dense Hydroxyapatite: A Review, Journal of Functional Biomaterials, 6 (2015) 1099-1140.
[22] A. Bigi, E. Boanini, M. Gazzano, 7 - Ion substitution in biological and synthetic apatites, in: C. Aparicio, M.-P. Ginebra (Eds.) Biomineralization and Biomaterials, Woodhead Publishing, Boston, 2016, pp. 235-266.
[23] A. Tricoteaux, E. Rguiti, D. Chicot, L. Boilet, M. Descamps, A. Leriche, J. Lesage, Influence of porosity on the mechanical properties of microporous β-TCP bioceramics by usual and instrumented Vickers microindentation, J. Eur. Ceram. Soc., 31 (2011) 1361-1369.
[24] R.D. Shannon, Revised effective ionic radii and systematic studies of interatomic distances in halides and chalcogenides, Acta Crystallographica Section A, 32 (1976) 751-767.
[25] C. Mellier, F. Fayon, V. Schnitzler, P. Deniard, M. Allix, S. Quillard, D. Massiot, J.-M. Bouler, B. Bujoli, P. Janvier, Characterization and Properties of Novel Gallium-Doped Calcium Phosphate Ceramics, Inorganic Chemistry, 50 (2011) 8252-8260.
[26] G. Renaudin, S. Gomes, J.-M. Nedelec, First-Row Transition Metal Doping in Calcium Phosphate Bioceramics: A Detailed Crystallographic Study, Materials, 10 (2017) 92.
[27] K. Matsunaga, T. Kubota, K. Toyoura, A. Nakamura, First-principles calculations of divalent substitution of Ca^{2+} in tricalcium phosphates, Acta Biomater., 23 (2015) 329-337.
[28] R.K. Singh, M. Srivastava, N.K. Prasad, S. Awasthi, A. Dhayalan, S. Kannan, Iron doped β-Tricalcium phosphate: Synthesis, characterization, hyperthermia effect, biocompatibility and mechanical evaluation, Mater. Sci. Eng. C, 78 (2017) 715-726.
[29] A. Bigi, E. Foresti, M. Gandolfi, M. Gazzano, N. Roveri, Isomorphous substitutions in β-tricalcium phosphate: The different effects of zinc and strontium, J. Inorg. Biochem., 66 (1997) 259-265.
[30] R. Singh, M. Srivastava, N.K. Prasad, S. Awasthi, A. Kumar Dhayalan, S. Kannan, Structural analysis and magnetic induced hyperthermia of Fe^{3+} and Mn^{2+} substituted β-$Ca_3(PO_4)_2$, New Journal of Chemistry, 41 (2017) 12879-12891.
[31] A. Jillavenkatesa, R.A. Condrate, The Infrared and Raman Spectra of β-and α-Tricalcium Phosphate (Ca3(Po4)2), Spectroscopy Letters, 31 (1998) 1619-1634.
[32] P.N. de Aza, C. Santos, A. Pazo, S. de Aza, R. Cuscó, L. Artús, Vibrational Properties of Calcium Phosphate Compounds. 1. Raman Spectrum of β-Tricalcium Phosphate, Chemistry of Materials, 9 (1997) 912-915.
[33] P.M.C. Torres, J.C.C. Abrantes, A. Kaushal, S. Pina, N. Döbelin, M. Bohner, J.M.F. Ferreira, Influence of Mg-doping, calcium pyrophosphate impurities and cooling rate on the allotropic α↔β-tricalcium phosphate phase transformations, J. Eur. Ceram. Soc., 36 (2016) 817-827.
[34] L. Sinusaite, I. Grigoraviciute-Puroniene, A. Popov, K. Ishikawa, A. Kareiva, A. Zarkov, Controllable synthesis of tricalcium phosphate (TCP) polymorphs by wet precipitation: Effect of washing procedure, Ceram. Int., 45 (2019) 12423-12428.
[35] B.C. Cornilsen, R.A. Condrate, The vibratonal spectra of β-Ca2P2O7 and γ-Ca2P2O7, Journal of Inorganic and Nuclear Chemistry, 41 (1979) 602-605.
[36] L. Sinusaite, A.M. Renner, M.B. Schuetz, A. Antuzevics, U. Rogulis, I. Grigoraviciute-Puroniene, S. Mathur, A. Zarkov, Effect of Mn doping on the low-temperature synthesis of tricalcium phosphate (TCP) polymorphs, J. Eur. Ceram. Soc., 39 (2019) 3257-3263.
[37] C. Stahli, J. Thuring, L. Galea, S. Tadier, M. Bohner, N. Dobelin, Hydrogen-substituted β-tricalcium phosphate synthesized in organic media, Acta Crystallogr., Sect. B, 72 (2016) 875-884.
[38] A. Abragam, B. Bleaney, Electron Paramagnetic Resonance of Transition Ions, Clarendon Press, Oxford, UK, 1970.
[39] J.A. Weil, J.R. Bolton, Electron Paramagnetic Resonance, Wiley2007.
[40] G. Morin, D. Bonnin, Modeling EPR Powder Spectra Using Numerical Diagonalization of the Spin Hamiltonian, Journal of Magnetic Resonance, 136 (1999) 176-199.

[41] S. Gomes, A. Kaur, J.M. Greneche, J.M. Nedelec, G. Renaudin, Atomic scale modeling of iron-doped biphasic calcium phosphate bioceramics, Acta Biomater., 50 (2017) 78-88.
[42] G. Renaudin, S. Gomes, J.M. Nedelec, First-Row Transition Metal Doping in Calcium Phosphate Bioceramics: A Detailed Crystallographic Study, Materials, 10 (2017) 92.
[43] A.M. Bishay, L. Makar, Role of Iron in Calcium Phosphate Glasses, J. Am. Ceram. Soc., 52 (1969) 605-609.
[44] I. Ardelean, C. Andronache, C. Cimpean, P. Pascuta, EPR and magnetic investigation of calcium-phosphate glasses containing iron ions, J. Optoelectron. Adv. Mater., 8 (2006) 1372-1376.
[45] J. Kliava, EPR of impurity ions in disordered solids distributions of the spin hamiltonian parameters, physica status solidi (b), 134 (1986) 411-455.
[46] S.Y. Park, S.K.M. Perikamana, J.H. Park, S.W. Kim, H. Shin, S.P. Park, H.S. Jung, Osteoinductive superparamagnetic Fe nanocrystal/calcium phosphate heterostructured microspheres, Nanoscale, 9 (2017) 19145-19153.
[47] T. Ates, S.V. Dorozhkin, O. Kaygili, M. Kom, I. Ercan, N. Bulut, F. Firdolas, S. Keser, N.C. Gursoy, I.H. Ozercan, Y. Eroksuz, T. İnce, The effects of Mn and/or Ni dopants on the in vitro/in vivo performance, structural and magnetic properties of β-tricalcium phosphate bioceramics, Ceram. Int., 45 (2019) 22752-22758.
[48] M.E. Zilm, L. Yu, W.A. Hines, M. Wei, Magnetic properties and cytocompatibility of transition-metal-incorporated hydroxyapatite, Mater. Sci. Eng. C, 87 (2018) 112-119.
[49] A. Vertes, D.L. Nagy, Mössbauer spectroscopy of frozen solutions, Akadémiai Kiadó, Budapest, 1990.
[50] D.H. Jones, K.K.P. Srivastava, Many-state relaxation model for the M\"ossbauer spectra of superparamagnets, Phys. Rev. B, 34 (1986) 7542-7548.
[51] M.A. Chuev, Multi-level relaxation model for describing the Mossbauer spectra of single-domain particles in the presence of quadrupolar hyperfine interaction, J. Phys.-Condes. Matter, 23 (2011) 11.
[52] C. Shuai, P. Feng, L. Zhang, C. Gao, H. Hu, S. Peng, A. Min, Correlation between properties and microstructure of laser sintered porous β-tricalcium phosphate bone scaffolds, Science and Technology of Advanced Materials, 14 (2013) 055002.
[53] R. Ghosh, R. Sarkar, Synthesis and characterization of sintered beta-tricalcium phosphate: A comparative study on the effect of preparation route, Mater. Sci. Eng. C, 67 (2016) 345-352.

Institute of Solid State Physics, University of Latvia as the Center of Excellence has received funding from the European Union's Horizon 2020 Framework Programme H2020-WIDESPREAD-01-2016-2017-TeamingPhase2 under grant agreement No. 739508, project CAMART².

Supporting information

Fe and Zn co-substituted beta-tricalcium phosphate (TCP): Synthesis, structural, magnetic, mechanical and biological properties

Lauryna Sinusaite[1], Anton Popov[1,2], Andris Antuzevics[3], Kestutis Mazeika[4], Dalis Baltrunas[4], Jen-Chang Yang [5], Shengfang Shi[6], Tohru Sekino[6], Aivaras Kareiva[1], Aleksej Zarkov[1,*]

[1]*Institute of Chemistry, Vilnius University, Naugarduko 24, LT-03225 Vilnius, Lithuania*

[2]*Department of Immunology, State Research Institute Centre for Innovative Medicine, Santariskiu 5, LT-08406 Vilnius, Lithuania*

[3]*Institute of Solid State Physics, University of Latvia, Kengaraga 8, LV-1063 Riga, Latvia*

[4]*State Research Institute Center for Physical Sciences and Technology, Vilnius LT-02300, Lithuania*

[5]*Graduate Institute of Nanomedicine and Medical Engineering, College of Biomedical Engineering, Taipei Medical University, 250 Wu-Hsing St, Taipei 11052, Taiwan*

[6]*The Institute of Scientific and Industrial Research, Osaka University, 8–1 Mihogaoka, Ibaraki, Osaka 567–0047, Japan*

**Corresponding author: E-mail: aleksej.zarkov@chf.vu.lt; +37062190153*

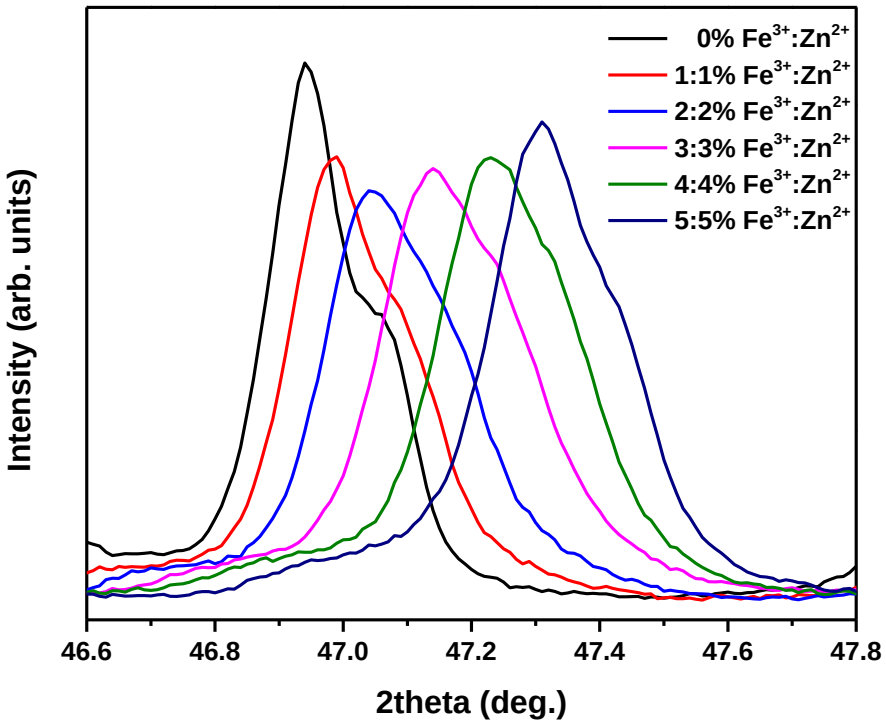

Fig. S1. XRD patterns of β-TCP powders with different amounts of Fe and Zn.

Table S1. Lattice parameters of β-TCP powders with different amounts of Fe and Zn.

Sample	Lattice parameter a (Å)	Lattice parameter b (Å)	Lattice parameter c (Å)	Cell volume (Å^3)
0% Fe:Zn	10.42273	10.42273	37.33308	3512.268
1:1% Fe:Zn	10.4035	10.4035	37.32911	3498.945
2:2% Fe: Zn	10.3788	10.3788	37.28103	3477.868
3:3% Fe: Zn	10.35913	10.35913	37.23379	3460.304
4:4% Fe: Zn	10.34491	10.34491	37.17521	3445.384
5:5% Fe:Zn	10.32327	10.32327	37.13673	3427.431

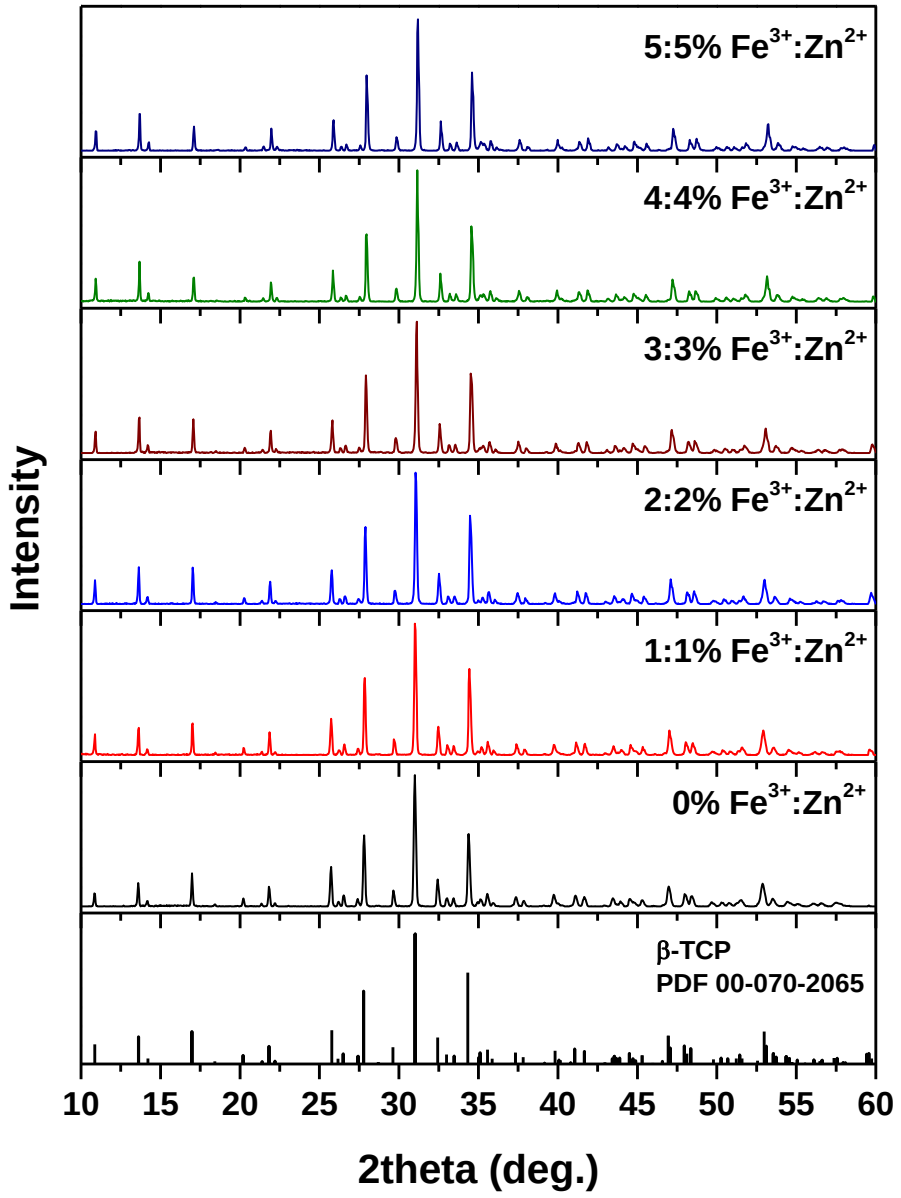

Fig. S3. XRD patterns of β-TCP ceramics with different amounts of Fe and Zn sintered at 1100 °C.

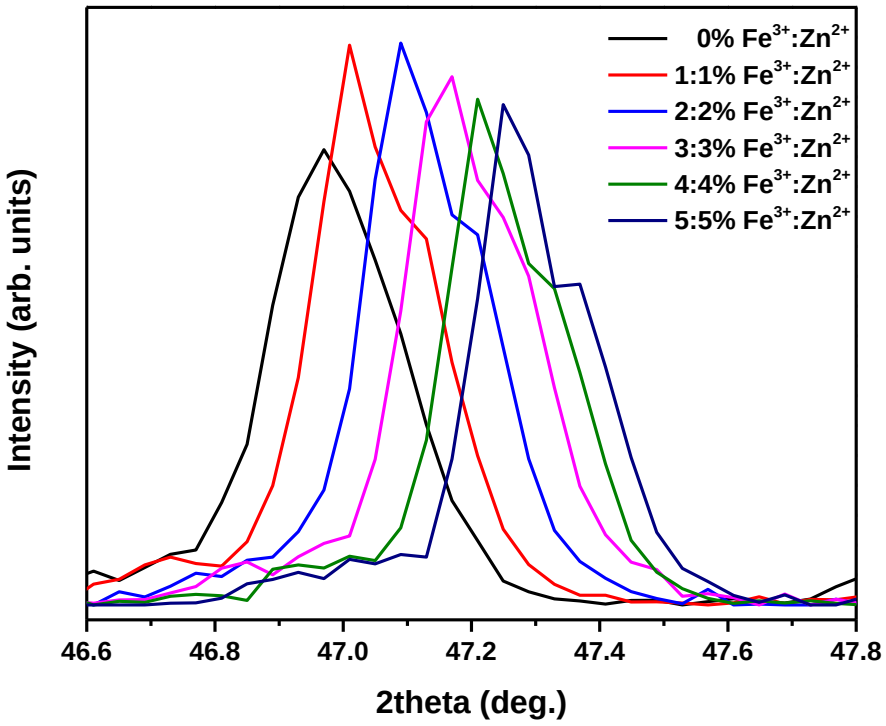

Fig. S4. XRD patterns of β-TCP ceramics with different amount of Fe^{3+} and Zn^{2+} ions sintered at 1100 °C.